Measurement 271 (2026) 120992

Contents lists available at ScienceDirect

Measurement

journal homepage: www.elsevier.com/locate/measurement

On-Device tilt and symmetry sensing with a MEMS Accelerometer: An Integration-Free embedded approach

Aliakbar Ghaderiaram *, Erik Eschlangen, Mohammad Fotouhi

Delft University of Technology, Delft, the Netherlands

ARTICLE INFO

Keywords:
MEMS Accelerometer
Tilt angle measurement
Embedded system
SHM

ABSTRACT

Field measurement of structural displacement and inclination is hindered by drift in double integration, stringent filtering needs, and the limited compute/bandwidth of low-cost microcontrollers. This work presents node based on an ADXL345 tri-axial accelerometer with on-board processing that estimates dynamic tilt and symmetry in real time without double integration. Three real-time filters, Butterworth IIR (BWF), finite impulse response (FIR), and moving average (MAF, uniform-tap FIR), were implemented on the device and benchmarked against an offline Savitzky–Golay reference. A rigid-body rotation model links off-centre acceleration to inclination and defines a dimensionless rotation index for symmetry assessment. Calibration against analytical motion identified a linear-phase FIR as optimal, yielding the lowest RMSE over 0.5–8 Hz while preserving waveform shape. Computational profiling on an 11.0592 MHz microcontroller measured average per-sample execution of 2.5 μs (MAF), 6 μs (FIR), and 12 μs (BWF), enabling 800 Hz local sampling with $\geq$ 100 Hz wireless streaming and an 8 $\times$ reduction via on-device decimation (no compression). Under cyclic tension, lateral acceleration quantified asymmetry: non-cracked and two-sided-cracked specimens showed comparable lateral levels, whereas one-sided-cracked specimens exhibited markedly higher values consistent with crack-induced rotation. Vertical acceleration agreed with acceleration reconstructed from displacement, with peak deviations of $\sim$ 9–14%; accuracy decreased at the lowest acceleration levels, consistent with stronger low-frequency spectral content. Tilt from acceleration tracked displacement-based tilt with minor underestimation at the smallest amplitudes. Overall, the node delivers embedded, phase-faithful filtering and tilt/symmetry estimation with quantified computational cost, making acceleration-based monitoring practical on resource-constrained hardware while avoiding big-data burdens.

1. Introduction

The advancement of Micro-Electro-Mechanical Systems (MEMS) accelerometers has significantly transformed the landscape of structural health monitoring (SHM) [1,2]. These compact, low-power, and cost-effective sensors now enable high-resolution dynamic and quasi-static measurements across diverse structural environments [3,4]. MEMS accelerometers have become critical components in monitoring transportation infrastructure, geotechnical hazards, underwater systems, and more [5–7]. Their ability to detect small structural movements, identify modal properties, and reconstruct displacement trajectories under ambient or operational loading conditions has driven their widespread adoption [2,8,9].

In railway systems, for instance, MEMS accelerometers such as the ADXL345 have been successfully mounted on sleepers at switches and crossings to monitor vertical motion under train loads [10]. These measurements help reveal variations in track stiffness, detect ballast voiding, and identify early signs of infrastructure degradation. It demonstrated that with a sampling rate up to 3200 Hz, the ADXL345 can capture acceleration histories that closely match geophone reference data, allowing for reliable displacement reconstruction. Similar success has been reported in modal analysis of bridges using wireless MEMS accelerometers, which enable scalable deployments and avoid the complexity of cabling [11,12].

Beyond surface transportation, MEMS accelerometers have enabled SHM in complex and otherwise inaccessible environments. In subsea applications, Ren et al. deployed MEMS accelerometer arrays to monitor 3D displacement of submarine pipelines during clamp-repair operations [13]. By estimating spatial attitudes relative to the gravity vector, these arrays provide real-time structural feedback where optical sensors fail

* Corresponding author.
E-mail address: a.ghaderiaram@tudelft.nl (A. Ghaderiaram).

https://doi.org/10.1016/j.measurement.2026.120992
Received 4 December 2025; Received in revised form 16 February 2026; Accepted 26 February 2026
Available online 27 February 2026

due to turbidity. In geotechnical and landslide-prone contexts, Najafabadi et al. designed surface micromachined MEMS sensors with enhanced sensitivity (0.3 pF/g) and low cross-axis interference (0.048%), tailored for weak-motion detection [14]. In seismic applications, MEMS-based accelerographs have proven capable of reliably capturing strong-motion waveforms for hazard mitigation [12].

Despite their versatility, MEMS accelerometers face critical challenges such as signal drift, quantization noise, and limited resolution for low-amplitude displacement monitoring [15]. These issues are particularly relevant for applications requiring displacement estimation via double integration of acceleration, where even minor baseline offsets can result in significant long-term integration error [14,16]. Consequently, the fidelity of displacement and inclination estimates hinges on careful signal preprocessing. To address these signal processing limitations a range of signal conditioning techniques have been evaluated. Low-pass and band-pass filters are foundational tools for attenuating irrelevant frequencies. Butterworth filters, typically second or third order with cutoff frequencies in the 0.1–25 Hz range are widely used for suppressing both high-frequency electrical noise and low-frequency baseline drift [12,17]. Finite Impulse Response (FIR) filters are commonly used during decimation in accelerometer signal processing to prevent aliasing and preserve linear-phase response. Zonta *et al.* [18] employed a 30th-order band-pass FIR (2.5–20 Hz) after decimating bridge acceleration data, ensuring accurate modal analysis without phase distortion. Similarly, Hong *et al.* [19] designed analytic FIR filters tailored for structural displacement reconstruction by fusing multi-rate signals, demonstrating the filter's effectiveness in alias-free decimation and signal fidelity retention.

Polynomial detrending, baseline correction, and zero-padding are essential preprocessing steps to stabilize double-integration results when deriving displacement and velocity from accelerometer data [15,20]. For example, baseline drift tends to amplify during integration, leading to large displacement errors, so preprocessing methods like linear or quadratic detrending are routinely used to mitigate this effect before applying numerical integration; this approach has been validated in accelerograph error studies using trapezoidal integration methods [21–23]. The trapezoidal rule is still the preferred integration technique due to its simplicity and acceptable accuracy, though it remains highly sensitive to DC bias and low-frequency noise components. Spectral analysis techniques, specifically the Fast Fourier Transform (FFT) and Welch's method for Power Spectral Density (PSD) estimation, are widely employed in SHM to evaluate the effectiveness of filtering stages and to identify structural modal frequencies and anomalies in acceleration data [22]. In this study, a fully integration-free pathway is pursued and validated against independent displacement- and tilt-based references; a direct benchmark against double-integration displacement is outside scope.

To enhance resolution, oversampling and digital averaging are increasingly adopted. For example, the ADXL345′s FIFO buffer supports oversampling at high rates (up to 3200 Hz), followed by digital averaging to reduce quantization noise [24]. This strategy has been shown to yield effective resolution gains of 1–2 bits, critical for applications requiring sub-milligravity sensitivity [10].

Yet, most signal–processing strategies are executed offline in tools like MATLAB or Python. Real-time deployment on embedded microcontrollers (MCU) remains rare. In contrast, Whelan *et al.* [25] implemented real-time oversampling and FIR filtering within a wireless smart sensor, including interrupt-driven digital filtering routines for accelerometer data. More recently, Moallemi *et al.* [26] demonstrated that real-time Butterworth and FIR filters can run efficiently on an STM32L4 MCU as part of an anomaly–detection pipeline in bridge health monitoring. These studies show that, with careful design, embedded real-time signal processing is practical even on constrained hardware.

This study develops and validates a compact MEMS accelerometer node that estimates dynamic tilt and symmetry directly from tri-axial acceleration on a low-cost MCU, without double integration. The contributions are: an on-device filtering chain benchmarked against an offline reference and culminating in a linear-phase FIR; a rigid-body rotation model for an off-centre sensor with a rotation index to quantify asymmetry; a quantified computational cost showing real-time feasibility and reduced data transmission; and an experimental validation on non-cracked (NC), one-side-cracked (OSC), and two-side-cracked (TSC) specimens, where lateral acceleration and the rotation index reveal crack-induced asymmetry and tilt from acceleration agrees with displacement-based tilt. Together, these results show that accelerometer-only, on-device tilt/symmetry estimation is practical with quantified accuracy and compute margins, enabling scalable, low-power SHM without double integration.

2. Methodology

2.1. Sensor node

2.1.1. Hardware and embedded software

The sensor node combines a low-power 8-bit MCU (ATmega328P) with an ADXL345 three-axis digital MEMS accelerometer connected over I^2C. The ADXL345 provides selectable range/bandwidth, high-resolution mode, a 32-sample FIFO, and reliable operation up to 3200 Hz, features exploited for burst acquisition and oversampling. A Bluetooth (HC-05) link enables wireless streaming to a host. Power is supplied via a lithium-ion battery. The electronics are integrated on a compact PCB suitable for attachment to test specimens (see Fig. 1(b, c)). On boot, the MCU configures the ADXL345 for high-resolution $\pm$ 16 g and a nominal 800 Hz local sampling. Data are acquired in interrupt-driven bursts when the FIFO crosses a watermark, minimizing CPU load. Each burst is time-stamped, passed through on-device filtering, packetized, and sent over UART to the Bluetooth module. During live Bluetooth streaming, the effective throughput is ≈100 Hz, constrained by the link. A lightweight MATLAB receiver parses binary packets, reconstructs time-stamped acceleration vectors, and provides live visualization and data logging. Optional post-processing utilities (e.g., spectral inspection) were available, but displacement via double integration was not used in this study.

All on-device filters run in fixed point with 16-bit inputs/coefficients and 32-bit accumulators (Q15/Q1.14) with saturation; multi-byte (16/32-bit) arithmetic is handled in software, the ATmega328P's hardware 8 × 8 multiplier supports efficient 16 × 16 → 32-bit multiply–accumulate operations (MACs), and post-shift normalization plus saturation guards prevent overflow.

Before analysis, each axis is bias/scale corrected using a 2 s stationary average for bias, a quick two-pose check (face-up/side) for scale, and a quiet-window detector that periodically re-zeros bias in operation (values stored in EEPROM).

2.1.2. Signal processing and filtering

Accurate use of tri-axial acceleration for tilt and symmetry metrics requires suppressing out-of-band noise and low-frequency drift while preserving waveform shape and timing [27,28]. On the MCU, three real-time digital filters were implemented: moving average (MAF, uniform-tap FIR) [29], Butterworth IIR (BWF) [30], and a designed FIR filter (non-uniform coefficients) [31]. Although MAF is formally an FIR filter (uniform coefficients), it is reported separately here as a minimal-compute FIR baseline, whereas "FIR" refers to a designed FIR with non-uniform coefficients. An offline Savitzky–Golay (SG) filter (MATLAB) was used only as a reference to benchmark signal fidelity and guide parameter tuning; it was not deployed on the MCU [32].

Samples are taken every T_s seconds ($f_s = 1/T_s$). Let x[n] be the input sample and y[n] the filtered output.

MAF: The MAF operates by convolving the signal with a rectangular window of length W, defined as Equation (1) [33]:

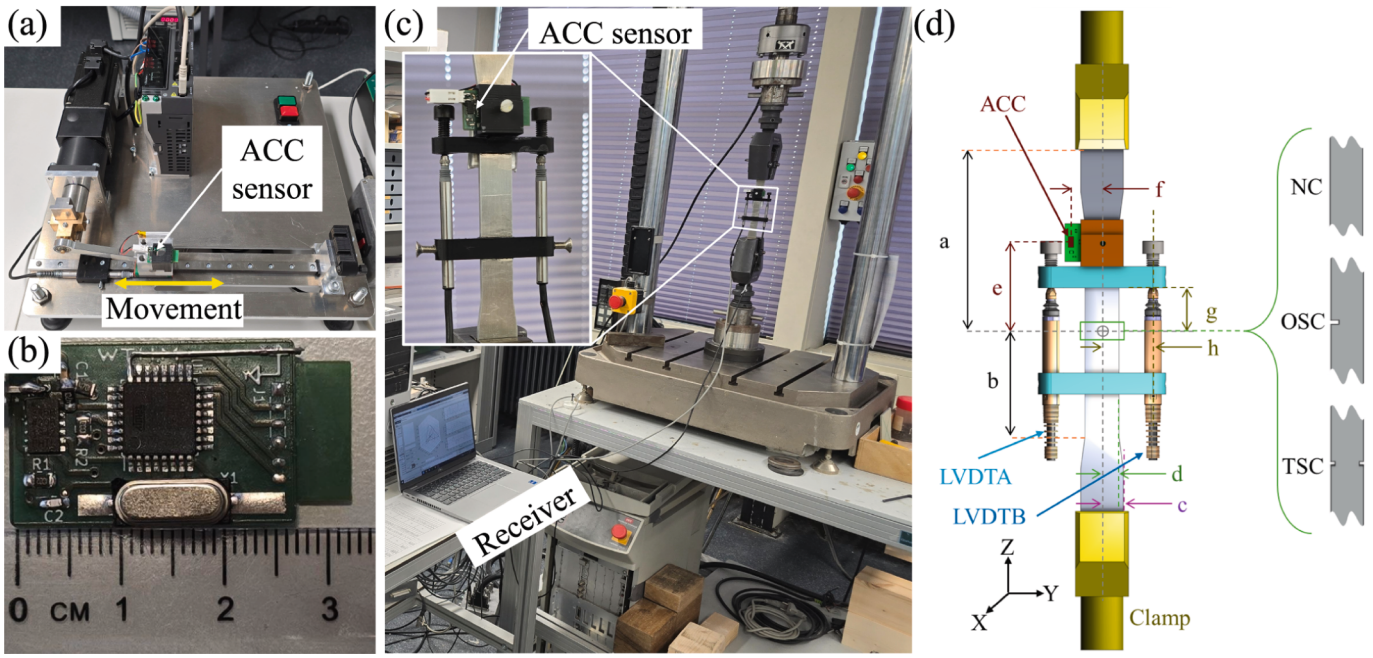

Fig. 1. (a) Setup for sensor calibration using a reciprocating platform, (b) the integrated MEMS-based wireless sensor node, (c) tensile test configuration under cyclic loading of the dog-bone specimen, and (d) schematic illustration of the specimen with the mounted accelerometer (ACC) and two LVDTs for displacement tracking, three different specimens (NC, OSC and TSC) are shown as well.

$$y[n] = \frac{1}{W}\sum_{k=0}^{W-1} x[n-k] \tag{1}$$

The rectangular window yields a sinc-shaped magnitude response; simple and low-cost, but with poor frequency selectivity and non-flat passband.

BWF: The Butterworth low pass has a maximally flat passband [34] and, in discrete time, is modelled by Equation (2):

$$y[n] = \sum_{k=0}^{N} b_k x[n-k] - \sum_{k=0}^{N} a_k y[n-k] \tag{2}$$

where N is the filter order, $n \in \mathbb{Z}$ is the sample index ($t = n \cdot T_s$) and $a_0 = 1$. The b_k is feedforward coefficient and a_k is feedback coefficient defining the recursive part of the filter. A maximally flat passband improves amplitude fidelity, but the recursive form introduces non-linear phase (frequency-dependent delay).

FIR Filter: The implemented FIR filter uses a symmetric coefficient structure to ensure linear phase response, which preserves the waveform shape. Its general form is explained in Equation (3):

$$y[n] = \frac{1}{N}\sum_{k=0}^{M-1} h[k]x[n-k] \tag{3}$$

where h[k] is the filter coefficients and M is the total number of filter taps (filter order = M−1). The implemented FIR uses symmetric coefficients (h[k] = h[M-1-k]) to ensure linear phase (constant group delay) while allowing sharper transitions by increasing tap count [35]. All on-device filters run in fixed point with 16-bit inputs/coefficients and 32-bit accumulators with saturation; FIR uses symmetric taps to reduce MACs, and BWF is realized as cascaded transposed biquads with power-of-two prescaling to prevent overflow, with outputs rescaled to Q15.

2.1.3. Accuracy

Filter accuracy is evaluated later using: (i) RMSE with respect to an offline SG reference, and (ii) qualitative checks of amplitude/phase preservation in the band of interest. Here are summarized analytical properties relevant to design:

- MAF: low computational cost; magnitude response with sinc-shaped main lobe and significant side lobes; limited frequency selectivity; non-flat passband.
- BWF: maximally flat passband magnitude; recursive realization with frequency-dependent (non-linear) phase; stability depends on coefficient quantization and structure.
- FIR (symmetric taps): linear phase (constant group delay); stability by construction (non-recursive); transition sharpness increases with taps; symmetric designs reduce multiplications.

2.1.4. Computational cost

For real-time, on-device operation, computational cost and memory footprint are decisive. SG, while accurate and shape-preserving, was used offline only due to high complexity and memory demand. On the MCU, MAF, BWF, and FIR were implemented in fixed-point arithmetic. To enable a fair comparison, BWF (order 6) and FIR (order 5; 6 taps) were tuned to similar passband characteristics; MAF used a window of 20 as a representative smoothing/latency trade-off. Table 1 summarizes per-sample operation counts and memory for standard realizations suitable for fixed-point MCUs (MAF with running-sum; BWF in transposed biquad form; FIR with symmetric taps). These counts reflect best-practice implementations and serve as hardware-agnostic estimates [36–38]; cycle-level timing on the MCU (11.0592 MHz) is reported in the Results. Frequency-response comparisons of MAF, designed FIR, and Butterworth filters are well established and can be found in standard DSP literature; therefore, we do not repeat Bode-style analyses here. The sensor node operates entirely in the time domain on a resource-constrained MCU, so we evaluate the filters using time-domain accuracy metrics and on-device resource occupancy. This ensures the comparison reflects embedded real-time behaviour rather than theoretical transfer-function characteristics.

In summary, MAF is computationally the most lightweight, FIR offers high signal fidelity with linear phase, and BWF provides a balance. For implementation on the MCU the FIR filter (with a small tap count)

Table 1
Per-sample computational cost and memory usage (matched for ~ 2nd order behaviour).

Filter	Multiplications	Additions	Memory (Samples)	Remarks
MAF (N = 20)	1 (or 0*)	19	2	Efficient via running sum
BWF (order 6)	15	12	6	Requires past input/output
FIR (6-tap or order 5)	6	5	6	Linear phase, no feedback

*Using a running sum method, MAF eliminates division and reduces the cost to one addition and one subtraction per sample.
MAF: Its simplicity and minimal memory needs make it suitable for low-power MCUs. With a sliding window, arithmetic cost becomes negligible, at the expense of limited frequency selectivity.
BWF: A compact realization with acceptable computational burden. The recursive structure requires careful coefficient scaling and saturation handling in fixed-point to avoid instability; phase is non-linear. It remains an efficient choice in SHM when phase linearity is not critical [39].
FIR: With taps matched to the BWF configuration, computational cost remains moderate while providing linear phase and numerical stability. Although sharper roll-off requires higher order, the symmetric-tap design reduces multiplications and preserves timing, advantageous for tilt/symmetry metrics [38].

provides the best trade-off between performance and feasibility. It ensures phase linearity and stable execution using fixed-point arithmetic while maintaining manageable memory and CPU load, making it the most suitable option for real-time SHM signal processing in this context.

2.1.5. Displacement estimation and inclination effects

The transformation of acceleration measurements into displacement is a key objective in SHM applications where direct measurement of displacement is infeasible [40]. This transformation typically requires two numerical integrations of the raw acceleration signal. The double-integration pathway is outlined for completeness, but the experiments in this study do not compute displacement; all results rely on tilt from acceleration and the rotation/symmetry index derived directly from triaxial acceleration. However, due to the inherent sensitivity of integration to low-frequency noise and bias, the process must be carefully handled using appropriate signal conditioning and integration strategies [41]. Given an acceleration signal a(t), the velocity v(t) and displacement x(t) can be obtained as explained in Equation (4).

$$v(t) = \int a(t)dt + C_1, x(t) = \int v(t)dt + C_2 \tag{4}$$

where C_1 and C_2 are constants of integration representing the initial velocity and displacement, respectively. These constants are typically set to zero or estimated from boundary conditions when known. In discrete-time implementation, the trapezoidal rule is commonly used due to its simplicity and moderate accuracy. Equation (5) calculates the velocity v[n] and displacement x[n] from a discrete acceleration signal a[n] sampled at interval T_S.

$$\begin{aligned} v[n] &= v[n-1] + \frac{T_S}{2}(a[n] + a[n-1]) \\ x[n] &= x[n-1] + \frac{T_S}{2}(v[n] + v[n-1]) \end{aligned} \tag{5}$$

This recursive method is computationally efficient and memory-light, making it suitable for MCU-based embedded systems. Nonetheless, to minimize integration errors, the acceleration signal must be pre-processed through filtering, zero-padding, and baseline correction. Polynomial detrending is often applied after integration to remove residual drift caused by noise or sensor bias.

2.1.6. Inclination angles derived from Triaxial acceleration measurements

In structural systems equipped with tri-axial MEMS accelerometers, apparent acceleration components can arise not only from translational motion but also from changes in the sensor's orientation due to tilt or inclination. Such static or dynamic angular deviations can project components of the gravitational acceleration vector along the sensing axes, thereby affecting the recorded signals even in the absence of structural motion [42].

Assuming the structure is loaded primarily in the vertical direction (Z-axis), a static inclination or slow rotation about the horizontal axes (X or Y) causes a measurable shift in the recorded accelerations along the orthogonal directions. The inclination angle θ with respect to the vertical axis can be estimated from the acceleration vector as explained in Equation (6) [42]:

$$\theta_x(t) = \tan^{-1}\left(\frac{a_y(t)}{a_z(t)}\right), \theta_y(t) = \tan^{-1}\left(\frac{a_x(t)}{a_z(t)}\right) \tag{6}$$

where a_x, a_y, a_z represent the measured acceleration components along the X, Y, and Z axes, respectively, and θ_x, θ_y denote inclination angles around the X and Y axes. These inclination angles cause lateral displacement in off-centre points. For a point located at a perpendicular distance h from the central vertical axis (neutral axis), the angular-induced displacement in the lateral plane u_y and u_x are given by Equation (7):

$$u_y(t) = h \bullet \sin(\theta_x(t)) \approx h \bullet \theta_x(t), u_x(t) = h \bullet \sin(\theta_y(t)) \approx h \bullet \theta_y(t) \tag{7}$$

The derivations use $\tan\theta \approx \theta$ and $\sin\theta \approx \theta$ (radians). The relative error for $\tan\theta \approx \theta$ is $< 0.3\%$ at 5°, ≈1.0% at 10°, and ≈2.3% at 15°. All tests here had $\theta \leq 1^\circ$. For applications exceeding ~5°, it is better to use the exact relations, $\theta = \arctan(a_y/a_z)$ and retain $\tan(\theta), \sin(\theta)$ in the geometry, without changing the rest of the formulation. While Equation (7) provides a geometric estimation of the lateral movement caused by tilt. While not used for long-term static tilt evaluation, this formulation supports dynamic symmetry analysis and was leveraged in this study to interpret rotation-induced acceleration in off-centre sensors.

2.1.7. Dynamic rotation and Off-Center sensor Modelling

To account for the influence of specimen rotation on the accelerometer response, the coupled motion of the specimen and the sensor is analytically modelled by considering both translational and rotational components of acceleration. When the specimen experiences bending or asymmetric deformation, the accelerometer positioned at a distance (a + e) from the fixed pivot point and with an offset f from the specimen's vertical centre experiences a combination of rigid-body and angular accelerations. Let the instantaneous angular displacement of the specimen be θ(t) and the vertical translation be $z_{rig}(t)$. The absolute displacement of the sensor in the local coordinate frame of the accelerometer can be described by Equation (8).

$$\begin{cases} a_y(t) \approx \underbrace{\ddot{y}_{rig}(t)}_{lateraltranslation \approx 0} + \underbrace{(a+e) \bullet \ddot{\theta}(t)}_{tangentialaboutpivot} \\ a_z(t) \approx \underbrace{\ddot{z}_{rig}(t)}_{verticaltranslation} - \underbrace{f \bullet \ddot{\theta}(t)}_{tangentialaboutpivot} \end{cases} \tag{8}$$

Because the excitation is primarily vertical, the lateral translational term $\ddot{y}_{rig}(t)$ is approximately zero. The two components correspond respectively to (i) the lateral acceleration due to the sensor's offset f from the rotation axis, and (ii) the vertical motion of the specimen's neutral axis combined with the rotational contribution at height (a + e). Depending on the direction convention, the sign of $a_y(t)$ may appear negative; in this work, positive $a_y(t)$ denotes motion toward the sensor's positive Y-axis.

Under small-angle rotation, Equation (8) fully describe the

instantaneous kinematics of an accelerometer located off-centre in a rotating specimen. The measured accelerations $a_y(t)$ and $a_z(t)$ therefore contain coupled information about rigid-body translation and angular motion and rearranging the above relations allows separating the rigid-body and rotational terms as shown in Equation (9).

$$\ddot{\theta}(t) = \frac{a_y(t)}{(a+e)}$$
$$\ddot{z}_{rig}(t) = a_z(t) + \frac{f}{(a+e)} a_y(t) \tag{9}$$

This enables direct estimation of angular and rigid-body accelerations from the raw accelerometer signals, without numerical integration or frequency-domain transformations. To quantify the relative contribution of rotation with respect to the translational response, a rotation index of accelerometer (R_{ACC}) is defined as a normalized measure of angular-to-rigid acceleration in the time domain in Equation (10).

$$R_{ACC}(t) = \left| \frac{\ddot{\theta}(t)}{\ddot{z}_{rig}(t)} \right| = \left| \frac{a_y(t)}{(a+e) \bullet a_z(t) + f \bullet a_y(t)} \right| \tag{10}$$

The $R_{ACC}(t)$ has a physical unit of [rad/m], representing angular acceleration per unit translational acceleration.

- Smaller values of $R_{ACC}(t)$ correspond to nearly pure translational or symmetric motion,
- intermediate values indicate coupled translation–rotation behaviour, and
- larger values signify strong rotational dominance or asymmetric deformation.

To analyse the sensitivity of $R_{ACC}(t)$ to sensor node placement error, $(a + e) \rightarrow (a + e) + \delta(a + e)$ and $f \rightarrow f + \delta f$, first order linearization of $R_{ACC}(t)$ gives Equation (11).

$$\frac{|\delta R|}{R} \approx \frac{|a_z|}{|(a+e)a_z + f a_y|} |\delta(a+a)| + \frac{|a_y|}{|(a+e)a_z + f a_y|} |\delta f|$$
$$= \frac{|\delta(a+e)| + |\tan\theta||\delta f|}{(a+e) + f\tan\theta} \tag{11}$$

where $\tan\theta = a_y/a_z$. Using the installed geometry $(a + e) = 0.113$ m, $f = 0.014$ m, and the observed angles (e.g., $\theta \approx 0.2^\circ$, $\tan\theta \approx 0.00349$), a $\pm$ 2 mm error yields $|\delta R|/R \approx 0.002/0.11305 \approx 1.8\%$ from the height term and $(0.00349 \times 0.002)/0.11305 \approx 0.006\%$ from the offset term. Even at $\theta = 2^\circ$, the offset contribution remains $\lesssim$0.06%. Thus, minor installation shifts do not compromise symmetry detection; height tolerance dominates while offset is negligible at small tilt.

This formulation provides a physically consistent and frequency-independent description of the sensor's dynamic response. It directly relates the instantaneous kinematics of the accelerometer to the structural deformation and can be evaluated entirely from time-domain signals.

2.2. Test setup

2.2.1. Sensor calibration

Sensor calibration was performed using a linear reciprocating test platform, as shown in Fig. 1(a). The integrated sensor node used in the calibration, shown in Fig. 1(b), includes the MEMS accelerometer, MCU, wireless transmitter, and on-board signal processing routines. The platform was designed to move the integrated accelerometer node along a controlled unidirectional path, simulating sinusoidal displacement profiles with predefined amplitudes (0.5 mm to 2 mm) and frequency range of 0.5 Hz to 8 Hz. The goal of this calibration procedure was to evaluate the raw output of the MEMS accelerometer and assess the performance of the implemented signal processing filters.

The displacement amplitude and frequency of the platform were configured via an external controller, and the actual movement was monitored using a reference Linear Variable Differential Transformer (LVDT). The accelerometer was mounted securely on the moving stage using a 3D-printed holder, ensuring a defined and repeatable orientation with respect to the global coordinate system. Data were recorded wirelessly using a custom-developed MATLAB application.

The collected raw acceleration signals were filtered using each selected filtering method (MAF, BWF, FIR) and then compared with the theoretical acceleration calculated by second derivative of the known input motion of the platform. This allowed for the identification of the most suitable filter settings for real-time estimation and evaluation of signal noise and drift under controlled conditions. This calibration phase also served to establish a baseline prior to deployment in the tensile test setup.

2.2.2. Cyclic tension–tension test

To evaluate the performance of the accelerometer-based monitoring under structural loading, a series of cyclic tensile tests were conducted on aluminum dog-bone specimens, as illustrated in Fig. 1(c) and Fig. 1(d). The specimens were clamped using mechanical grips, and a cyclic tension–tension force was applied using an Instron testing machine. Each cycle induced elastic elongation and potential rotation in the specimen due to a combination of factors, including fixture compliance, non-ideal clamping symmetry, and crack-induced asymmetry. Tests were performed using a minimum preload of 0.5 kN to ensure clamp engagement, and four different maximum loads of 2, 4, 6, and 8 kN in a sinusoidal profile. The frequency range was kept consistent with the calibration setup (0.5 Hz to 8 Hz) which targets the frequency band that typically dominates fatigue-relevant structural response in civil structures. Three types of specimens were tested: non-cracked, one-side cracked, and two-side cracked. The OSC samples contained a single 2 mm notch at mid-length on one side, while the TSC samples had two 2 mm notches symmetrically placed on both sides. These configurations were selected to explore how crack presence and location influence structural inclination during cyclic loading.

A custom-designed sensor node was mounted on the specimen surface using a 3D-printed holder as shown in Fig. 1(d), ensuring firm attachment throughout the loading process. The placement of the accelerometer was intentionally offset from the vertical and horizontal centerlines to facilitate the detection of inclination-induced acceleration components. Two LVDTs were positioned symmetrically on either side of the specimen to measure vertical displacement at locations equidistant from the central axis. Table 2 summarizes the key dimensional parameters of the specimen and the sensor placement shown in Fig. 1(d). These displacement signals provided a reference for estimating structural inclination and validating accelerometer-derived data.

The accelerometer recorded three-axis acceleration data throughout each loading cycle, transmitted wirelessly to the MATLAB interface for real-time processing and storage. The objective was to evaluate the sensor's ability to capture translational and rotational behavior, as well

Table 2
Dimensional specifications of the test specimens and sensor placement.

Parameter	Qty	Unit
a	75e-3	m
b	5e-2	m
c	1e-2	m
d	8e-3	m
e	38e-3	m
f	14e-3	m
g	2e-2	m
h	24e-3	m
Specimen thickness	3e-3	m
Specimen yield point[43]	≈15e + 3	N

as to quantify the accuracy of the derived inclination and displacement estimations under practical loading conditions.

3. Results and Discussion

3.1. Sensor calibration results

To assess the sensor node performance and accuracy and suitability of the embedded filtering techniques, a controlled sensor calibration test was conducted using the linear reciprocating platform illustrated in Fig. 1(a). The FFT results in Fig. 2(a) reveal the frequency content of the raw acceleration signal across all displacement levels (0.5 mm to 2 mm). As expected, the primary frequency peaks match the imposed excitation frequencies (0.5 Hz to 8 Hz), confirming the consistency of the test platform. The increasing harmonic content at larger displacement amplitudes highlights the growing importance of signal fidelity in preserving waveform shape, particularly when transitioning to displacement through double integration. At 0.5 Hz, the fundamental acceleration amplitude is smaller, so noise and leakage components become more prominent in relative terms. This is primarily due to the lower overall acceleration magnitude at low excitation frequencies, as explained in Equation (4).

Fig. 2(b) illustrates representative results from the calibration tests, comparing raw acceleration signals against filtered outputs from the MAF, BWF, and FIR filters. The SG filter is used as the accuracy baseline. The theoretical acceleration is also plotted in subfigures of Fig. 2(b) to to illustrate the sensor's fidelity relative to theoretical motion. Visual inspection of the signals indicates that MAF exhibits noticeable signal smoothing, particularly at higher frequencies, whereas BWF and FIR filters preserve signal dynamics more effectively. This observation is supported by the RMSE values (in m·s¯2) annotated at the end of each set of subplots. Because the filter outputs were acquired separately, signals were time-aligned to a common steady-state window prior to RMSE computation. Two effects explain the RMSE trend: (i) as excitation frequency increases, the true acceleration amplitude grows with f^2 for fixed displacement amplitude, so absolute RMSE in m·s^{-2} naturally rises even when relative error is similar; and (ii) the low-order embedded low-pass designs have finite transition bands, so as the fundamental approaches the 10 Hz cutoff, peak attenuation and slight waveform distortion further increase RMSE. At 8 Hz (near the passband edge), BWF and FIR show similar magnitude response and suppress higher harmonics similarly, leading to comparable RMSE after alignment.

The filters shown in Fig. 2(b) reflect optimized parameter settings obtained through systematic tuning. Filter parameters were tuned by sweeping order and cutoff/window settings. Fig. 3(a) summarizes RMSE (relative to SG) across the parameter sweeps. For the MAF, larger window sizes reduce high-frequency noise but excessively smooth the signal, leading to growing RMSE at higher excitation frequencies. For BWF and FIR filters, cutoff frequency and order were varied systematically. Fig. 3(a) illustrates that for the same filter order FIR filter performe lower RMSE and more important than that, FIR shows less dependancy to cuttoff frequencies than BWF. In Fig. 3(a), the cutoff f_c(for BWF/FIR)

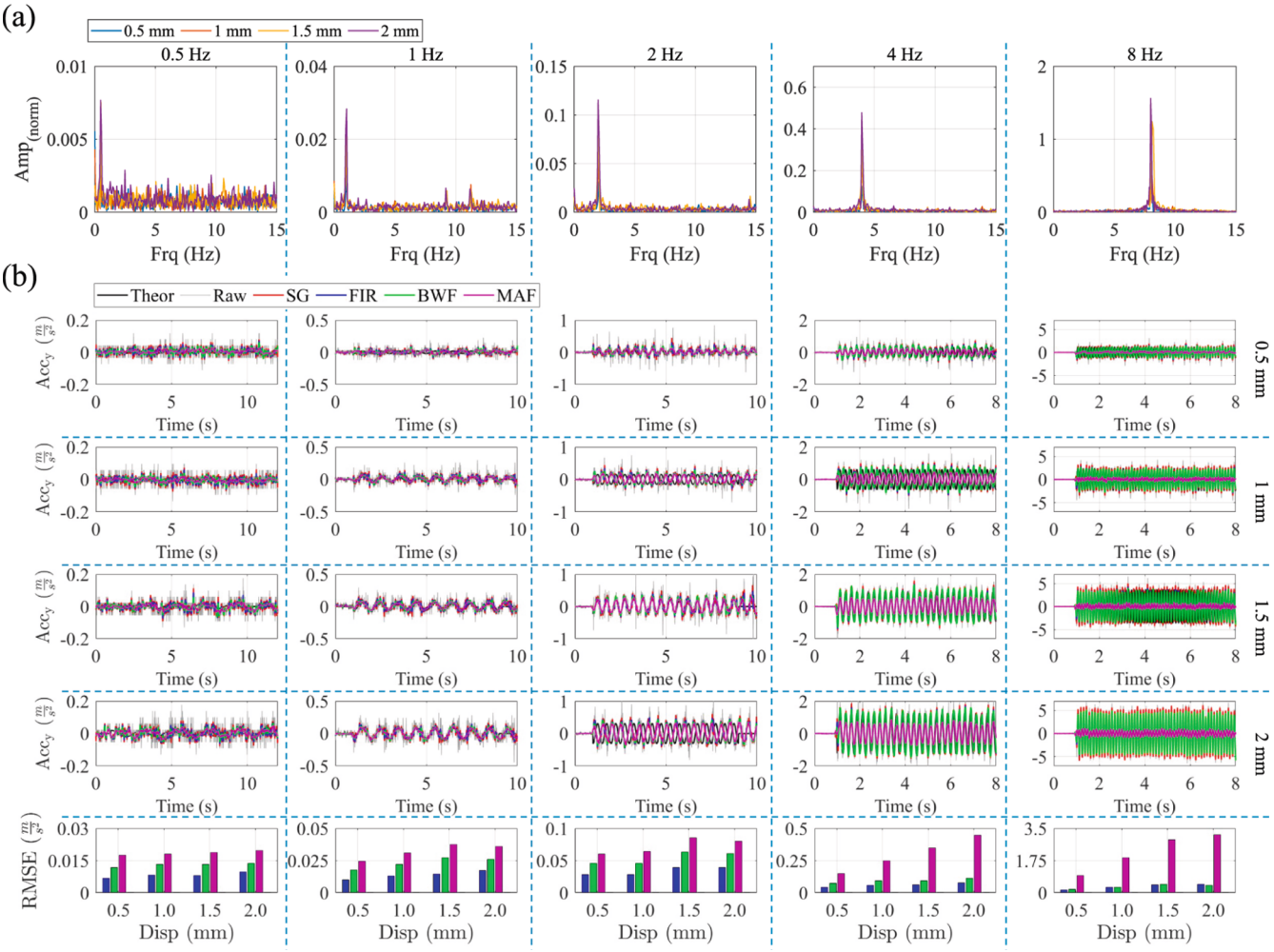

Fig. 2. (a) FFT of raw acceleration signals for different displacement amplitudes and frequencies, (b) Time-domain comparison of raw, SG, MAF, FIR, and BWF filters besides theoretical acceleration. RMSE bars (bottom row) show deviation from SG across displacement levels.

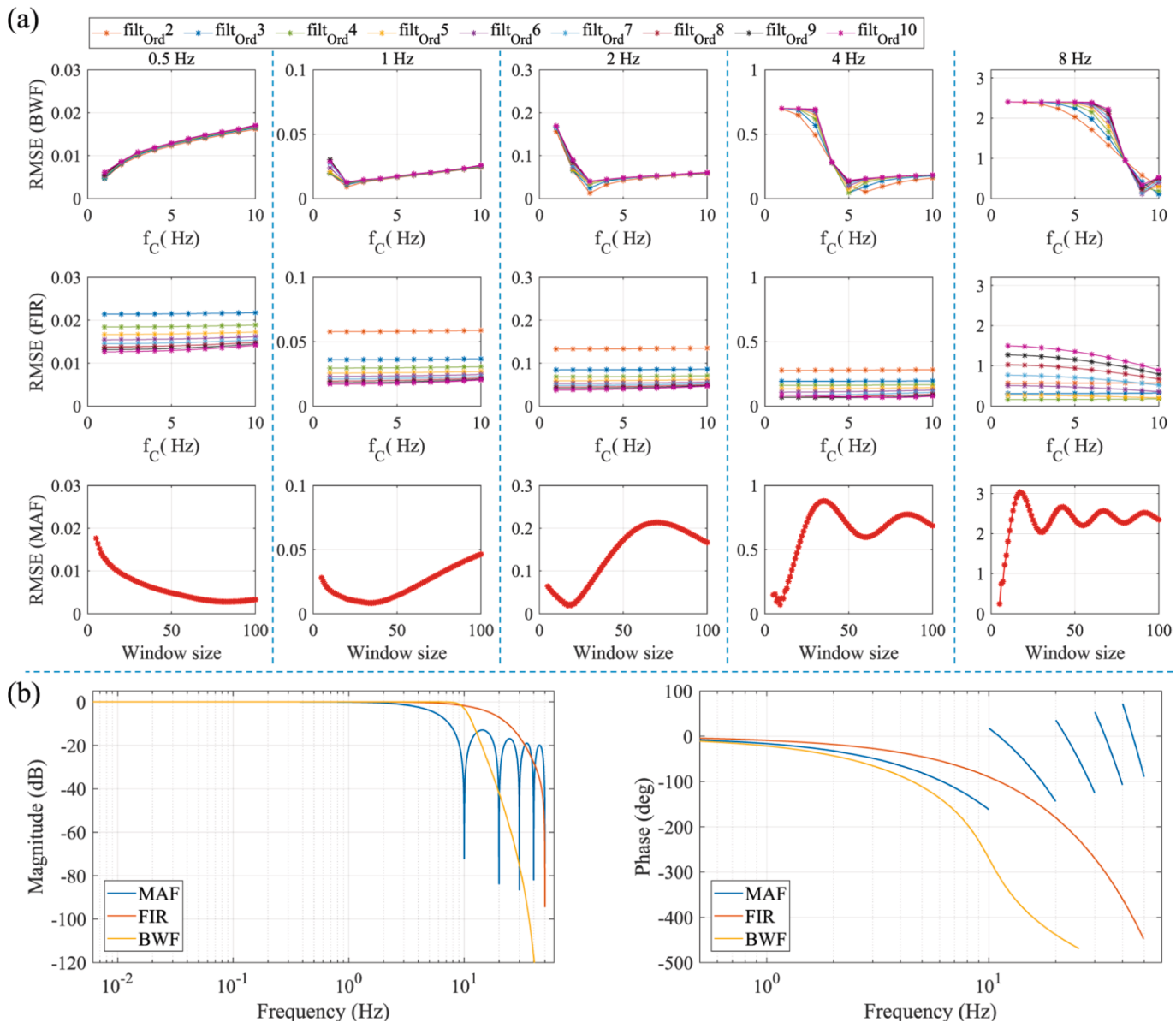

Fig. 3. (a) RMSE ($m \cdot s^{-2}$) versus cutoff f_c for BWF (top) and FIR (middle), and versus window size for MAF (bottom), at excitation frequencies 0.5–8 Hz. Curves are shown for filter orders 2–10 (BWF/FIR). RMSE is computed relative to SG-filtered acceleration. (b) Corresponding magnitude and phase responses of the implemented filters (MAF, FIR, BWF) in the live streaming configuration.

and the window size (for MAF) were swept below, near, and above the excitation to show how tuning affects accuracy across 0.5–8 Hz. These results motivated a single compromise for later tests.

Among the three filters, FIR consistently achieves the lowest RMSE values across the test range when appropriately tuned (see Fig. 2(b)). This is attributed to its linear phase response and sharper transition bands. However, BWF offers competitive performance with fewer computational resources. The MAF, while simplest, shows a marked decline in accuracy as frequency increases, supporting its use only in low-frequency applications or for basic smoothing.

Beyond accuracy, the computational cost of each filtering method was also checked to see if they can run in real-time on an ATmega328P MCU with an 11.0592 MHz clock. As shown in Fig. 4(a), Fig. 4(c), and Fig. 4(d), the MAF had the lowest demands in terms of memory use, number of operations, and execution time, making it best suited for simple applications or where signal dynamics are limited to low frequencies. The FIR filter needed more memory and calculations than MAF, yet it ran faster than BWF on the ATmega328P. This is because the 6-tap symmetric FIR evaluates three multiply–accumulate pairs into a single 32-bit accumulator with one final normalization and no feedback states, using a circular input buffer. By contrast, the order-6 BWF (three cascaded biquads) must load and update 32-bit state variables in each section, apply intermediate saturation/prescaling, and serialize the sections due to feedback, operations that incur additional multi-byte moves and shifts on an 8-bit core. These architecture effects explain the measured ≈6 μs/sample (FIR) versus ≈12 μs/sample (BWF) at 11.0592 MHz.

Additionally, Fig. 4(b) illustrates the computational cost of the SG filter across varying polynomial orders and frame lengths. The configuration used in this work (order 11, frame length 21), marked on the plot, corresponds to 42 operations per sample, comparable to a 10th-order BWF. However, Fig. 4(c) and Fig. 4(d) show that SG filtering requires substantially more memory and results in higher execution time, making it unsuitable for real-time deployment on resource-constrained MCUs.

These findings support the filter selection process and summarized in

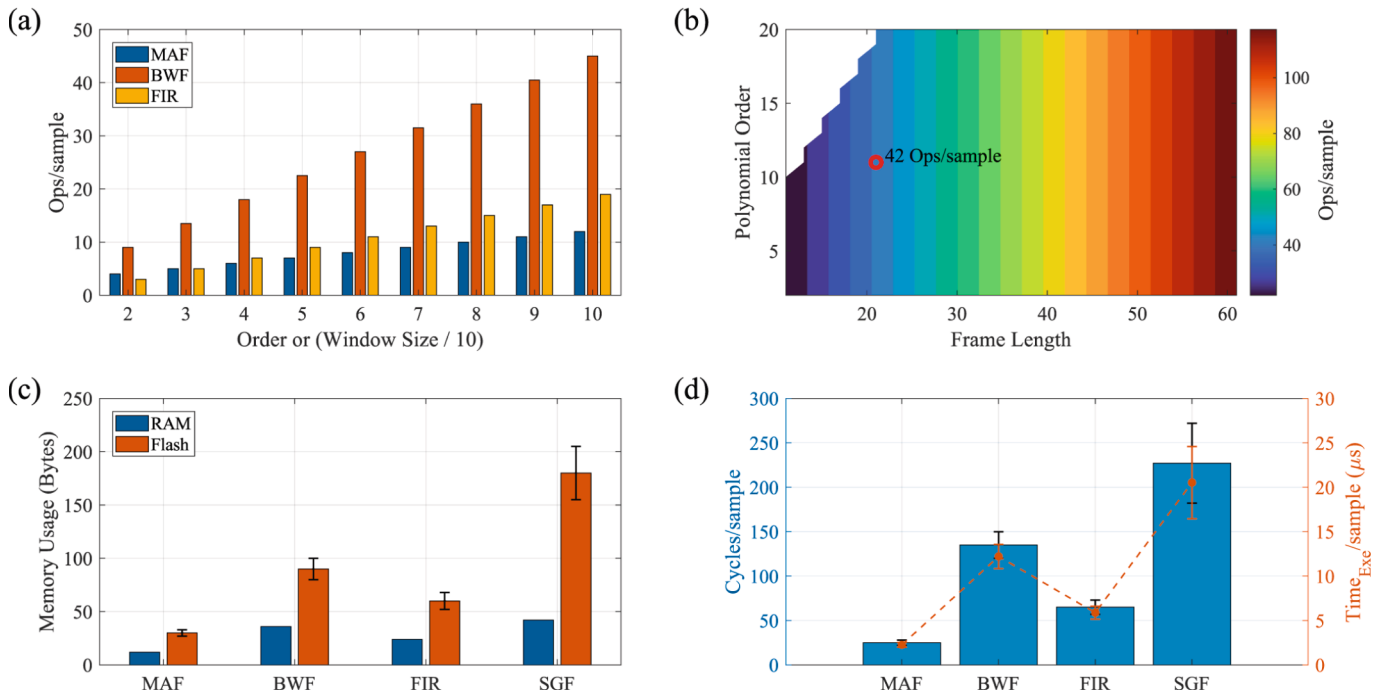

Fig. 4. (a) Operations per sample for MAF, BWF, and FIR filters across increasing order or window size. (b) SG filter complexity landscape showing operations per sample as a function of polynomial order and frame length; the configuration used in this work (order 11, frame length 21) is marked. (c) RAM and Flash memory usage for each filter. (d) CPU cycles and execution time per sample for each filter, based on 11.0592 MHz MCU.

Table 1. The FIR filter provides the best overall compromise between accuracy, stability, and resource efficiency, especially when implemented with low order. The calibration results directly set the signal-processing configuration used in the subsequent tensile tests: FIR, 10 Hz cutoff, order 5 (6 taps). The MAF and BWF traces in Fig. 3(a) are included to bound performance and compute cost; in particular, the MAF plots illustrate the expected high-frequency smoothing with larger windows and serve only as calibration benchmarks. All tensile-test analyses used the FIR setting above. To further clarify the trade-off between filtering performance and computational cost, Fig. 3(b) presents the corresponding magnitude and phase frequency responses of the implemented filters under the live streaming configuration. Although all filters were tuned to the same nominal cutoff, their frequency-domain characteristics differ: the Butterworth filter provides steeper attenuation but exhibits nonlinear phase behaviour, the FIR maintains near-linear phase with a wider transition band, and the MAF shows the characteristic sinc-type response. These distinctions are consistent with the observed differences in signal fidelity and resource utilization.

3.2. Tensile test observations

To evaluate the sensor node under realistic structural conditions, tensile tests were conducted on three specimen types: NC, OSC, and TSC. Each was subjected to sinusoidal loading at five frequencies (0.5–8 Hz) and four load amplitudes (2, 4, 6, and 8 kN). These tests aimed to assess the node's capability in capturing translational and lateral motion under increasingly asymmetric deformation states. The analysis focuses on acceleration in the Y and Z directions, as well as derived inclination angles, to identify variations in dynamic response due to crack-induced asymmetry. This section does not reconstruct displacement; instead, dynamic behaviour is quantified via acceleration-derived tilt and rotation index and cross-checked against tilt and acceleration reconstructed from displacement.

Fig. 5 presents the peak-to-peak lateral acceleration (ACC_Y) measured over time for different specimens under varying loading conditions. In both 4 Hz and 8 Hz cases (Fig. 5(a)–(b)), the NC and TSC specimens show similar levels of lateral acceleration, suggesting minimal inclination during cyclic loading, likely attributable to minor compliance in the clamped boundaries. In contrast, the OSC specimen exhibits significantly higher ACC_Y values, especially at elevated loads, as also evident in the full-range plot (Fig. 5(c)). This behaviour reflects the asymmetric geometry of the OSC specimen, where a single-sided crack causes dynamic inclination or tilt during cyclic loading. At 8 Hz the NC/TSC lateral peaks are near the noise floor; small cross-axis leakage from the large vertical component, minor fixture/notch misalignment, and reduced SNR explain the irregular pattern, whereas OSC remains monotonic because its tilt-driven lateral component is much larger. These results confirm the sensor node's ability to detect rotational or lateral asymmetry resulting from structural discontinuities.

To validate the vertical acceleration recorded by the sensor node, Fig. 6(a) compares the measured ACC_Z with acceleration derived from LVDT displacement signals under various loading conditions. The theoretical acceleration calculated from known loading levels of the NC specimen is also shown, demonstrating very close agreement with both the LVDT-derived and measured ACC_Z signals, serving as a strong validation for the accuracy of the sensor node in symmetric configurations.

Among the specimens, both OSC and TSC exhibit higher acceleration responses compared to NC, especially at increased loading levels. This is consistent with their reduced cross-sectional areas at the crack zone, due to the presence of either OSC or TSC of equal length, resulting in increased vertical displacements under the same external load. However, the measured signals in these cracked specimens also begin to diverge slightly from the LVDT-derived reference at higher frequencies, which is attributed to the additional rotational effects caused by the geometric asymmetry (notably in OSC), affecting the vertical acceleration sensed at the off-centre location.

To maintain figure clarity, these error bars are omitted from Fig. 6(a); nevertheless, the worst-case deviation is ~ 9–14%, which is acceptable within the scope of this study for SHM trend/asymmetry assessment.

To further investigate structural asymmetry and its dynamic effects, Fig. 6(b) presents the ratio of displacement amplitudes from LVDTA and

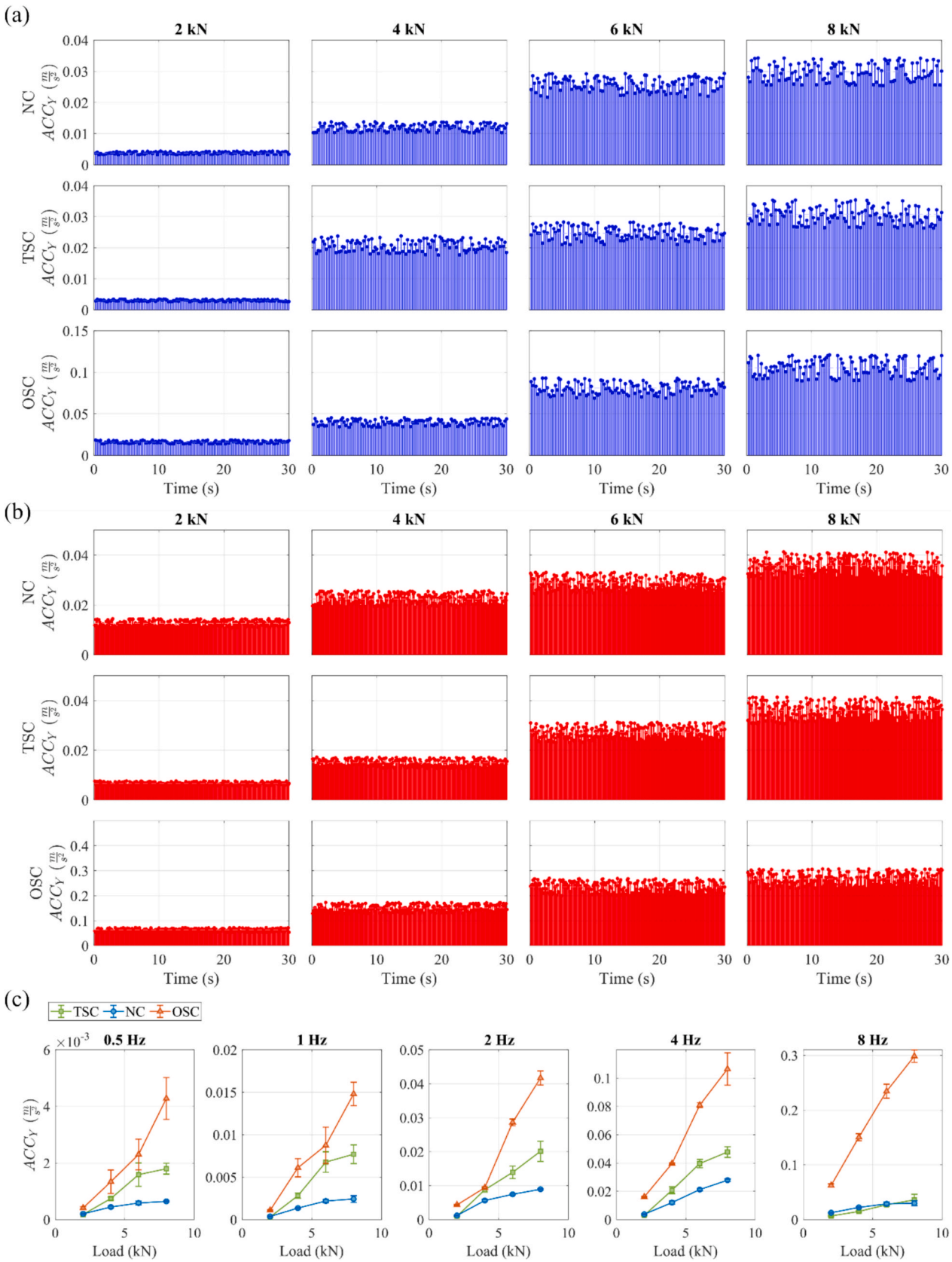

Fig. 5. Measured peak-to-peak lateral acceleration (ACC_Y) by the sensor node across different specimen types: (a) Time history at 4 Hz, (b) Time history at 8 Hz, and (c) Summary of peak-to-peak values over the full frequency range (0.5–8 Hz) for each loading level. Error bars indicate cycle-to-cycle variability.

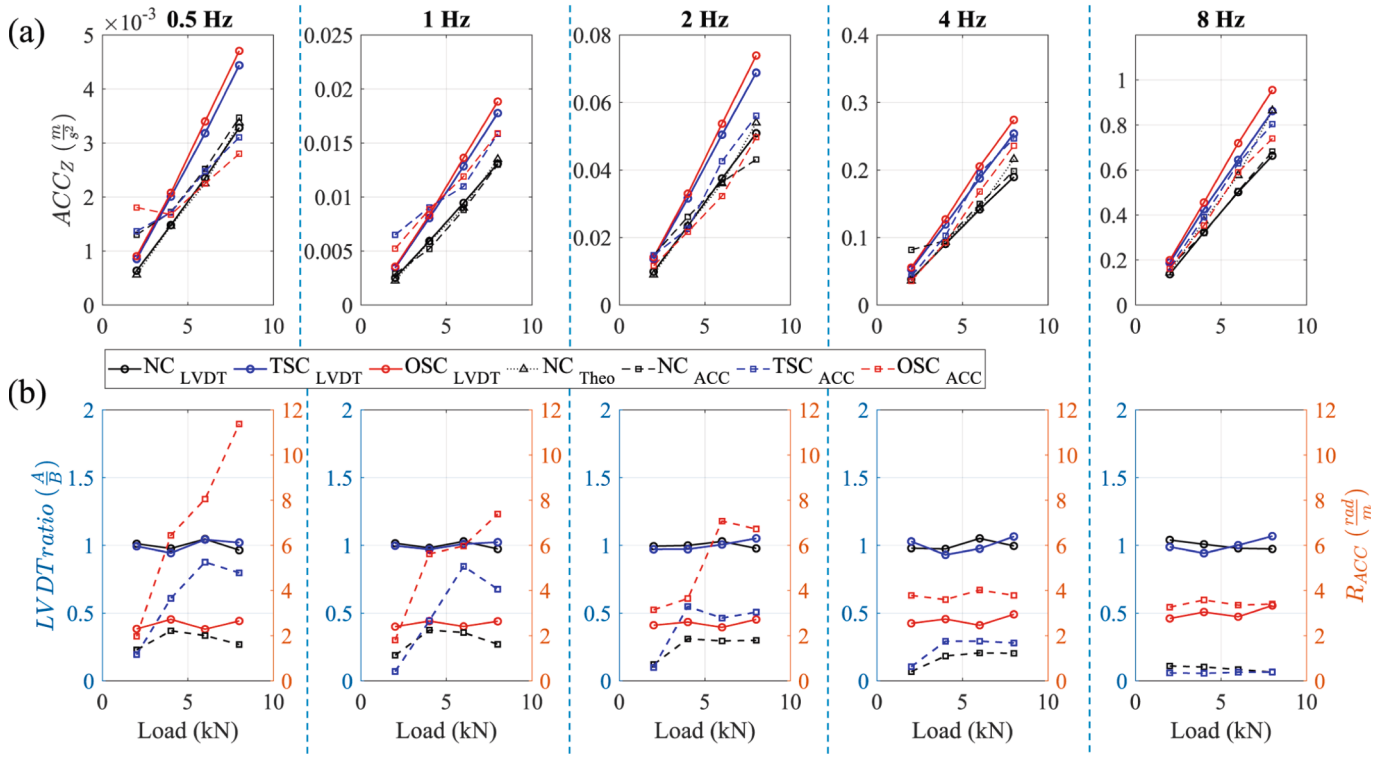

Fig. 6. (a) Vertical acceleration measured by the sensor node compared with acceleration derived from LVDT readings across all load levels and excitation frequencies, for different specimen types. (b) Left y-axis: LVDT amplitude ratio (A/B). Right y-axis: accelerometer-based rotation index RACC (rad/m) from Equation (10), versus applied load.

LVDTB alongside the accelerometer-derived rotation index R_{ACC}, as defined in Equation (10). In the plots, the left y-axis shows the LVDT A/B amplitude ratio, while the right y-axis shows R_{ACC} in (rad/m) computed from the lateral and vertical accelerations via Equation (10). The LVDT ratio reflects the extent of non-uniform axial elongation across the specimen's width, while R_{ACC} quantifies rotational effects based solely on the vertical and lateral acceleration components captured by the sensor node. For the NC and TSC specimens, the LVDT A/B ratio stays near one, and R_{ACC} remains low across most test conditions, consistent with symmetric geometry and balanced deformation. In contrast, the OSC specimen shows clear deviations from unity in both the LVDT ratio and R_{ACC}, especially at higher frequencies. This deviation reveals the presence of dynamic rotation induced by the asymmetric crack, which results in uneven strain distribution and tilt during cyclic loading. The close correspondence between these two independently measured quantities confirms the validity of the theoretical framework introduced in Section *Dynamic Rotation and Off-Center Sensor Modelling* and demonstrates the sensor node's ability to detect structural asymmetry without relying solely on displacement sensors.

As evident from Fig. 6(a) and Fig. 6(b), the node shows lower accuracy when acceleration amplitudes are small (low loads/low frequencies). In this regime, the true ACC amplitude approaches the ADXL345 noise floor, so the measurement is dominated by a near-constant noise level plus cross-axis leakage from the larger vertical component. Consequently, the fundamental at 0.5 Hz becomes less distinguishable, while small spectral components (noise and leakage-related harmonics) appear relatively larger, consistent with Fig. 2(a). The effect is specimen-dependent because the signal level differs, not because the sensor noise changes. For NC/TSC, the lateral/rotational component is intrinsically small and can fall near the noise floor, making the response sensitive to minor fixture compliance/misalignment. In OSC, the asymmetric crack produces a much larger tilt-driven lateral component, yielding a higher effective SNR and a more stable, monotonic trend.

To extract tilt angle under cyclic loading, θ_{ACC} was computed as $\arctan(ACC_Y/ACC_Z)$ per Equation (6) after band-limiting, while θ_{LVDT} was obtained from the differential displacement of the two LVDTs assuming uniform rotation between them (Fig. 7). At 4 Hz, NC and TSC show small, near-zero-mean θ that scales modestly with load, whereas OSC exhibits clearly larger θ that increases with load, consistent with crack-induced asymmetry. θ_{ACC} and θ_{LVDT} are generally in phase across loads, indicating consistent dynamics between inertial and displacement-derived estimates. At 8 Hz, the same pattern persists with slightly tighter agreement at higher loads; a mild underestimation by θ_{ACC} at the lowest load reflects reduced SNR, consistent with the low-acceleration regime highlighted by the spectral characteristics at 0.5 Hz in Fig. 2(a) (higher relative energy in undesired harmonics). Overall, the ACC-based method captures dynamic inclination with good fidelity, with accuracy improving as acceleration level increases.

4. Conclusions

This study shows that a compact MEMS accelerometer node can perform on-device estimation of dynamic tilt and rotational symmetry on a low-cost MCU, without double integration. A hardware-in-the-loop survey identified a linear-phase FIR (order 5, 10 Hz cutoff) as the preferred embedded filter, yielding the lowest error versus an offline reference while preserving waveform shape. Computational profiling on an 11.0592 MHz MCU (≈2–3 µs/sample MAF; ≈6 µs/sample FIR; ≈12 µs/sample BWF) confirms real-time feasibility with 800 Hz local sampling, about100 Hz wireless streaming, and reduced data transmission.

Under cyclic tension, lateral acceleration and the rotation index (R_{ACC}) sensitively revealed crack-induced asymmetry (OSC > NC≈TSC). Tilt from acceleration (θ_{ACC}) agreed with tilt reconstructed from displacement, and vertical acceleration matched displacement-derived acceleration with ~ 9–14% peak deviation; accuracy decreased only at the lowest acceleration levels, consistent with spectral contamination at low frequency. At 0.5 Hz, the low-SNR regime yields the largest

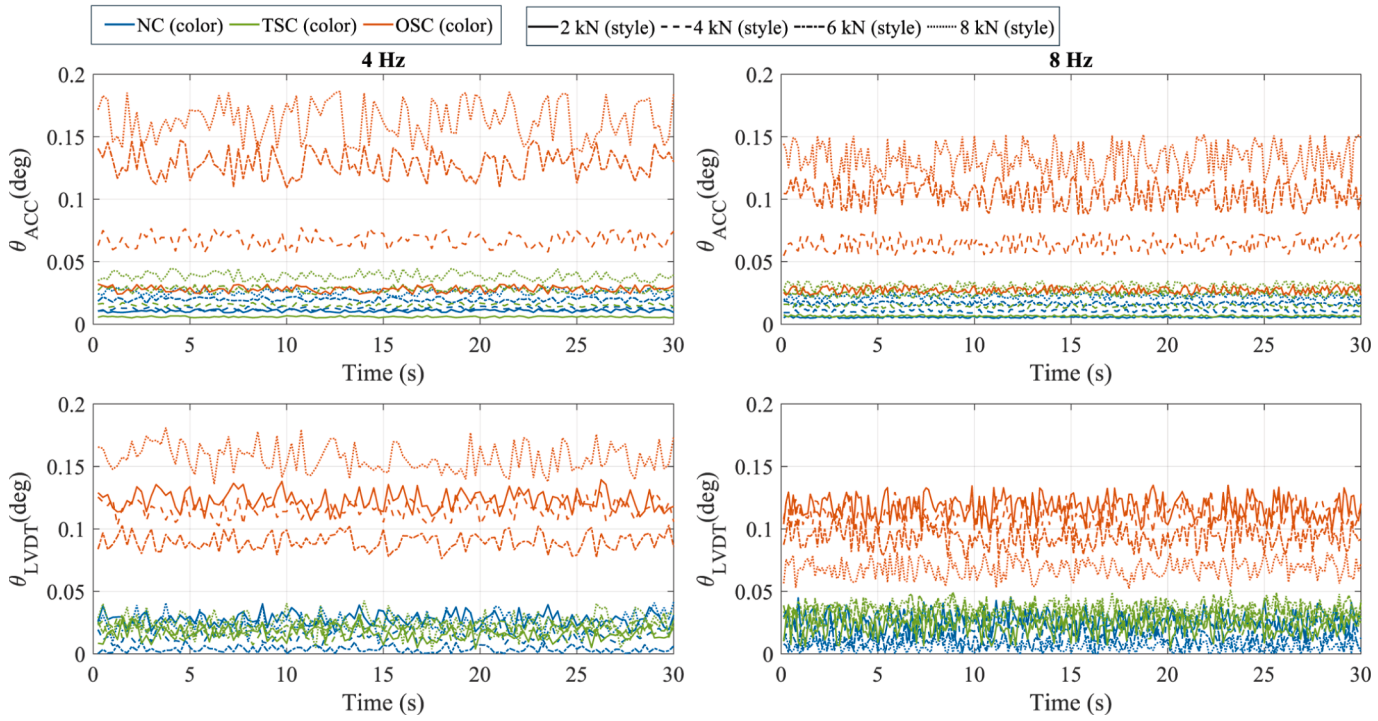

Fig. 7. Estimated tilt angle θ over time for two excitation frequencies (4 Hz and 8 Hz), calculated using (top row) the accelerometer-based method (θ_{ACC}) and (bottom row) LVDT-based measurements (θ_{LVDT}). Results are shown for all specimen types (NC, TSC, OSC) and four load levels (2, 4, 6, and 8 kN), with colours distinguishing specimens and line styles indicating load levels.

deviation (~9–14%), driven by the ADXL345 noise floor at 800 Hz local sampling rather than 8-bit arithmetic; a double-precision replay changed RMSE by < 1%. These outcomes validate the off-centre sensor model and demonstrate that accelerometer-only tilt/symmetry metrics can characterize structural behaviour robustly without displacement reconstruction, yielding lower drift risk, lower compute complexity, and lower data volume. Future work will target adaptive/multirate filtering, on-node bias mitigation, and fusion with gyroscopes to enhance low-g and high-frequency performance, and field studies to set decision thresholds for damage detection using θ_{ACC} and R_{ACC}.

5. Declaration of generative AI and AI-assisted technologies in the manuscript preparation process

During the preparation of this work, the authors used OpenAI's ChatGPT to assist with text refinement. All content generated with this tool was carefully reviewed, verified, and revised by the authors, who take full responsibility for the final manuscript.

CRediT authorship contribution statement

Aliakbar Ghaderiaram: Writing – original draft, Visualization, Validation, Software, Methodology, Investigation, Formal analysis, Data curation, Conceptualization. **Erik Eschlangen:** Supervision, Resources, Funding acquisition. **Mohammad Fotouhi:** Writing – review & editing, Supervision, Resources, Funding acquisition.

Declaration of competing interest

The authors declare that they have no known competing financial interests or personal relationships that could have appeared to influence the work reported in this paper.

Data availability

Data will be made available on request.

References

[1] B. Aygün, V.C. Gungor, Wireless sensor networks for structure health monitoring: recent advances and future research directions, Sens. Rev. 31 (2011) 261–276, https://doi.org/10.1108/02602281111140038/FULL/PDF.
[2] L. Zhu, Y. Fu, R. Chow, B.F. Spencer, J.W. Park, K. Mechitov, Development of a High-Sensitivity Wireless Accelerometer for Structural Health Monitoring, Sensors 2018, Vol. 18, Page 262 18 (2018) 262. DOI: 10.3390/S18010262.
[3] B.F. Spencer, J.W. Park, K.A. Mechitov, H. Jo, G. Agha, Next Generation Wireless Smart Sensors Toward Sustainable Civil Infrastructure, Procedia Eng. 171 (2017) 5–13, https://doi.org/10.1016/J.PROENG.2017.01.304.
[4] S. Hassani, U. Dackermann, A Systematic Review of Advanced Sensor Technologies for Non-Destructive Testing and Structural Health Monitoring, Sensors 2023, Vol. 23, Page 2204 23 (2023) 2204. DOI: 10.3390/S23042204.
[5] P. Negi, R. Kromanis, A.G. Dorée, K.M. Wijnberg, Structural health monitoring of inland navigation structures and ports: a review on developments and challenges, Struct. Health Monit. 23 (2024) 605–645, https://doi.org/10.1177/14759217231170742.
[6] M. Sun, Y. Liu, · Liuyuan Zhao, W. Xie, W. Mao, Advances and challenges in assessing submarine landslide risks to marine infrastructure, 121 (2025) 7811–7837. DOI: 10.1007/s11069-025-07113-6.
[7] M. Le Breton, F. Liébault, L. Baillet, A. Charléty, É. Larose, S. Tedjini, Dense and long-term monitoring of earth surface processes with passive RFID — a review, Earth Sci. Rev. 234 (2022) 104225, https://doi.org/10.1016/J.EARSCIREV.2022.104225.
[8] H. Hasani, F. Freddi, R. Piazza, F. Ceruffi, A Wireless Data Acquisition System Based on MEMS Accelerometers for Operational Modal Analysis of Bridges, Sensors 2024, Vol. 24, Page 2121 24 (2024) 2121. DOI: 10.3390/S24072121.
[9] S. Komarizadehasl, F. Lozano, J.A. Lozano-Galant, G. Ramos, J. Turmo, Low-Cost Wireless Structural Health Monitoring of Bridges, Sensors 2022, Vol. 22, Page 5725 22 (2022) 5725. DOI: 10.3390/S22155725.
[10] J.-Y.; Shih, P.; Weston, M.; Entezami, C.; Roberts, J.-Y. Shih, P. Weston, M. Entezami, C. Roberts, M. O'callaghan, Experiences Using MEMS Accelerometers on Railway Bearers at Switches and Crossings to Obtain Displacement—Awkward Situations, Infrastructures 2024, Vol. 9, Page 91 9 (2024) 91. DOI: 10.3390/INFRASTRUCTURES9060091.
[11] C. Bedon, E. Bergamo, M. Izzi, S. Noè, Prototyping and Validation of MEMS Accelerometers for Structural Health Monitoring—The Case Study of the Pietratagliata Cable-Stayed Bridge, Journal of Sensor and Actuator Networks 2018, Vol. 7, Page 30 7 (2018) 30. DOI: 10.3390/JSAN7030030.

[12] M.A. Bravo-Haro, X. Ding, A.Y. Elghazouli, MEMS-based low-cost and open-source accelerograph for earthquake strong-motion, Eng. Struct. 230 (2021) 111675, https://doi.org/10.1016/J.ENGSTRUCT.2020.111675.
[13] X. Ren, J. Chen, P. Zhou, Z. Jin, H. Ge, Y. Si, Y. Zhang, X. Peng, X. Chen, Y. Peng, In-situ monitoring of clamp-repair-induced displacements in the submarine pipeline using a MEMS accelerometer array: a sea trial, Ocean Eng. 316 (2025) 119905, https://doi.org/10.1016/J.OCEANENG.2024.119905.
[14] H.R. Najafabadi, T.G. Goto, T.C. Martins, M.S.G. Tsuzuki, A. Barari, Designing MEMS accelerometer for enhanced sensitivity and reduced cross-sensitivity in landslide monitoring, Measurement 226 (2024) 114092, https://doi.org/10.1016/J.MEASUREMENT.2023.114092.
[15] D.M. Boore, Effect of Baseline Corrections on Displacements and Response Spectra for Several Recordings of the, Chi-Chi, Taiwan, Earthquake, Bull. Seismol. Soc. Am. 91 (2001) (1999) 1199–1211, https://doi.org/10.1785/0120000703.
[16] M. Crognale, C. Rinaldi, F. Potenza, V. Gattulli, A. Colarieti, F. Franchi, Developing and Testing High-Performance SHM Sensors Mounting Low-Noise MEMS Accelerometers, Sensors 2024, Vol. 24, Page 2435 24 (2024) 2435. DOI: 10.3390/S24082435.
[17] G. Zheng, Y. Tian, W. Zhao, S. Jia, N. He, Band-Stop Filtering Method of Combining Functions of Butterworth and Hann Windows to Ultrasonic Guided Wave, J. Pipeline Syst. Eng. Pract. 13 (2022) 04021076, https://doi.org/10.1061/(ASCE)PS.1949-1204.0000621/ASSET/99755BC9-DCD7-480A-89E4-83495B051874/ASSETS/IMAGES/LARGE/FIGURE14.JPG.
[18] E. Favarelli, E. Testi, A. Giorgetti, The impact of sensing parameters on data management and anomaly detection in structural health monitoring, J Civ Struct Health Monit 12 (2022) 1413–1425, https://doi.org/10.1007/S13349-022-00566-4/FIGURES/12.
[19] Y.H. Hong, S.G. Lee, H.S. Lee, Design of the FEM-FIR filter for displacement reconstruction using accelerations and displacements measured at different sampling rates, Mech. Syst. Signal Process. 38 (2013) 460–481, https://doi.org/10.1016/J.YMSSP.2013.02.007.
[20] R. Ferrero, F. Gandino, M. Hemmatpour, B. Montrucchio, M. Rebaudengo, Exploiting accelerometers to estimate displacement, 2016 5th Mediterranean Conference on embedded Computing, Student Challenge, MECO, 2016 (2016), pp. 206–210.
[21] S.C. Stiros, Errors in velocities and displacements deduced from accelerographs: an approach based on the theory of error propagation, Soil Dyn. Earthq. Eng. 28 (2008) 415–420, https://doi.org/10.1016/J.SOILDYN.2007.07.004.
[22] E.T. Lee, H.C. Eun, Y.J. Choi, Y.J. Ahn, S.G. Lee, S.W. Park, Structural performance experiment by moving cart to mount measurement sensors, Journal of Vibroengineering 18 (2016) 1157–1166, https://doi.org/10.21595/JVE.2016.16544.
[23] L. Chiominto, G. D'Emilia, A. Gaspari, E. Natale, Dynamic Multi-Axis Calibration of MEMS Accelerometers for Sensitivity and Linearity Assessment, Sensors (basel) 25 (2025) 2120, https://doi.org/10.3390/S25072120.
[24] J.F. Christopher, L. James, Utilization of the First In, First Out (FIFO) Buffer in Analog Devices, Inc. Digital Accelerometers, n.d.
[25] M.J. Whelan, K.D. Janoyan, Design of a robust, high-rate wireless sensor network for static and dynamic structural monitoring, J. Intell. Mater. Syst. Struct. 20 (2009) 849–863, https://doi.org/10.1177/1045389X08098768;PAGE:STRING:ARTICLE/CHAPTER.
[26] A. Moallemi, A. Burrello, D. Brunelli, L. Benini, Exploring Scalable, Distributed Real-Time Anomaly Detection for Bridge Health Monitoring, IEEE Internet Things J 9 (2022) 17660–17674, https://doi.org/10.1109/JIOT.2022.3157532.
[27] C.J. Fisher, Using an Accelerometer for Inclination Sensing, n.d.
[28] C. Jonscher, P. Helming, D. Märtins, A. Fischer, D. Bonilla, B. Hofmeister, T. Grießmann, R. Rolfes, Dynamic displacement measurement of a wind turbine tower using accelerometers: tilt error compensation and validation, Wind Energy Sci. 10 (2025) 193–205, https://doi.org/10.5194/WES-10-193-2025.
[29] J. Kluga, E. Grabs, T. Chen, A. Ancans, M. Stetjuha, D. Rjazanovs, A. Ipatovs, Motion Sensors Data Fusion for Accurate Measurement in AHRS Systems, 2024 Photonics and Electromagnetics Research Symposium, PIERS 2024 - Proceedings (2024). DOI: 10.1109/PIERS62282.2024.10618677.
[30] W.Z. Wang, Y.W. Guo, B.Y. Huang, G.R. Zhao, B.Q. Liu, L. Wang, Analysis of filtering methods for 3D acceleration signals in body sensor network, in: Proceedings of 2011 International Symposium on Bioelectronics and Bioinformatics, ISBB, 2011 (2011), pp. 263–266, https://doi.org/10.1109/ISBB.2011.6107697.
[31] R.K. Prasad, Performance of improved FIR filer using FPGA, International Journal of Recent Technology and Engineering (IJRTE) 8 (2019) 6022–6024, https://doi.org/10.35940/IJRTE.D8056.118419.
[32] S. Gesemann, TrackFit: Uncertainty Quantification, Optimal Filtering and Interpolation of Tracks for Time-Resolved Lagrangian Particle Tracking, 14th International Symposium on Particle Image Velocimetry 1 (2021). DOI: 10.18409/ISPIV.V1I1.92.
[33] S.W. Smith, Moving Average Filters, Digit Signal Process (2003) 277–284, https://doi.org/10.1016/B978-0-7506-7444-7/50052-2.
[34] N. Stamenković, S. Stamenković, M. Dejanović, D. Dejanović, Transition between flat magnitude and flat group delay low pass recursive digital filters, The University Thought - Publication in Natural Sciences 9 (2019) 62–66. DOI: 10.5937/UNIVTHO9-20907.
[35] Anon, Splitting the unit delay, IEEE Signal Process Mag. 13 (1996) 30–60, https://doi.org/10.1109/79.482137.
[36] R.G. Lyons, Understanding Digital Signal Processing, Prentice Hall PTR, 2004.
[37] J.G. Proakis, D.K. Manolakis, Digital Signal Processing, Prentice Hall, 2006.
[38] S.W. Smith, The scientist and engineer's guide to digital signal processing, California Technical Publishing, 1997.
[39] M.J. Whelan, M.V. Gangone, K.D. Janoyan, R. Jha, Real-time wireless vibration monitoring for operational modal analysis of an integral abutment highway bridge, Eng. Struct. 31 (2009) 2224–2235, https://doi.org/10.1016/J.ENGSTRUCT.2009.03.022.
[40] T. Wu, L. Tang, X. Zhang, Y. Liu, X. Li, Z. Zhou, An improved Structural Displacement monitoring Approach by Acceleration-aided Tilt Camera Measurement, Struct. Control Health Monit. 2023 (2023) 6247516, https://doi.org/10.1155/2023/6247516.
[41] D.J. Grover, Low-frequency drift reduction in the integration of repetitive signals, in: Proceedings of the Institution of Electrical Engineers 113, 1966, p. 895, https://doi.org/10.1049/PIEE.1966.0149.
[42] J.K. Lee, E.J. Park, S.N. Robinovitch, Estimation of attitude and external acceleration using inertial sensor measurement during various dynamic conditions, IEEE Trans. Instrum. Meas. 61 (2012) 2262–2273, https://doi.org/10.1109/TIM.2012.2187245.
[43] A. Ghaderiaram, R. Mohammadi, E. Schlangen, M. Fotouhi, Development of an innovative Extension for Fatigue Life monitoring using a Piezoelectric Sensor, Procedia Struct. Integrity 52 (2024) 570–582, https://doi.org/10.1016/J.PROSTR.2023.12.057.